ELSEVIER

# Thermal and chemical kinetic characterization of multiphase and multicomponent substances by laser heating

Ashot Nazarian [a], Cary Presser [b],*

[a] Science Applications International Corporation, Vienna, VA 22182, United States
[b] National Institute of Standards and Technology, Gaithersburg, MD 20899-8360, United States

## Abstract

A novel approach is described that determines the thermal behavior and decomposition of multiphase solid and liquid substances, such as chemical wastes, fuels, aerosol particles, and propellants through rapid and controlled heating with laser radiation. The laser-driven thermal reactor (LDTR) was developed to provide near temporally resolved determination of substance thermophysical properties and chemical reaction characteristics over a wide range of temperatures (up to 2000 K), heating rates (up to several hundreds of degrees per second), gas pressures, and ambient environments. Described is the experimental arrangement and supporting theory that is used to determine substance thermophysical and chemical behavior. Examples of the application of this technique are given for different substances, namely, a simulant multicomponent organic chemical waste, nitromethane, and activated carbon.
Published by Elsevier Ltd.

## 1. Introduction

Optimization and efficient operation of different high-temperature processes, such as the energy generation from conventional and renewable fuels, and thermal treatment of wastes and propellants, can benefit from in situ, temporally resolved thermal characterization (i.e., thermophysical properties, chemical reaction mechanisms, and chemical kinetic rates) of these substances. Determination of the thermal properties of substances, whether gas, liquid, solid, or a combination of phases is available with conventional techniques such as thermal optical analysis, thermogravimetric analysis, differential scanning calorimetry, and others. To illustrate their application to substance thermal heating, the differential scanning calorimeter is appropriate for relatively small size samples (<20 mg), low temperatures (<800 K), and low heating rates (a few degrees per minute) [1]. Thus, the technique is appropriate

for modeling thermal processes initiated by relatively low energy events under near steady-state conditions.

Energetic wastes are composed of a complex multiphase mixture of organics, solvents, additives, and a variety of other inorganic substances [1]. Determination of the potential for release of such wastes to the environment, as caused by a rapid release of chemical energy, is a difficult and complex problem. Such a release can be caused by several factors, such as a thermally accelerating runaway reaction, and/or high-energy initiator (e.g., lightning or fire). How such waste mixtures behave and react during exposure to a high-energy initiator, and what are the chemical reaction byproducts, can be of great concern. The behavior of these substances can be dependent on many parameters, including the substance physical and chemical properties, as well as the properties of the surrounding environment. The screening tool used presently to determine the potential of a waste for such a reaction is the differential scanning calorimeter (DSC). The DSC and other conventional thermal analysis techniques are appropriate for temperature levels up to 1000 K and heating rates up to 1 K/s.

---

* Corresponding author.
 *E-mail address:* cpresser@nist.gov (C. Presser).

## Nomenclature

| | |
|---|---|
| $A$ | sample geometric cross-sectional area |
| $C$ | calibration constant (usually in the range of 1.0 to 1.5) |
| $c_p$ | specific heat |
| $d$ | sample diameter |
| $d_c$ | characteristic path length through the sample |
| $(dT/dt)_D$ | temperature decay |
| $(dT/dt)_R$ | temperature rise |
| $(dT/dt)_{R1}, (dT/dt)_{R2}$ | sample-temperature derivatives |
| $E$ | exponential coefficient in units of absolute temperature |
| $E_a$ | activation energy |
| $F(T,T_0)$ | heat transfer term |
| $\Delta H$ | enthalpy |
| $I$ | intensity of the laser beam that heats the sample |
| $k$ | imaginary part of the complex refractive index; coverage factor |
| $k_a$ | Arrhenius expression |
| $k_0, q_0$ | pre-exponential coefficients |
| $\ell$ | characteristic distance of the thermal loss from the sample surface |
| $m$ | sample total initial mass |
| $m_c$ | mass of the reactive portion of the sample |
| $n$ | sample number |
| $q(T)$ | specific heat release rate due to chemical reaction |
| $q_c$ | sample thermal loss by conduction |
| $q_r$ | thermal loss by radiation |
| $q_{tc}$ | conductive thermal loss through the thermocouple wire |
| $Q$ | total specific heat release (or absorption) |
| $R$ | universal gas constant (8.314 J K$^{-1}$ mol$^{-1}$) |
| $R_1(T_r)$ | rate at which heat is transferred from the reactor at temperature $T_r$ |
| $R_2(T)$ | rate of heat loss from the sample and substrate |
| $s$ | standard deviation |
| $t$ | time |
| $t_{1/2}$ | characteristic time for the temperature to rise to half of its maximum value |
| $T$ | sample/substrate temperature |
| $T_g$ | gas temperature |
| $T_{max}$ and $T_0$ | steady-state sample temperatures defined in Fig. 4a |
| $T_r$ | reactor temperature |
| $T_1, T_2$ | sample temperatures |
| $u_c$ | combined standard uncertainty |
| $x$ | sample thickness |

*Greek symbols*

| | |
|---|---|
| $\alpha$ | sample absorption coefficient |
| $\alpha_d(T)$ | thermal diffusivity |
| $\beta(T)$ | absorptivity |
| $\varepsilon(T)$ | emissivity |
| $\kappa(T)$ | thermal conductivity |
| $\lambda$ | wavelength |
| $\rho$ | density |
| $\sigma$ | Stefan–Boltzmann constant (5.67 $\times$ 10$^{-8}$ W m$^{-2}$ K$^{-4}$) |
| $\tau$ | temperature-dependent relaxation time |

However, we have found (from unpublished results) that conventional techniques can fail to detect important chemical processes and phenomena, and sample thermal characteristics because of the lack of temporal resolution during substance decomposition when heated to higher temperatures. As an example, sodium nitrate ($NaNO_3$) and sodium nitrite ($NaNO_2$) chemically decompose at relatively slow heating rates of 5 K/min at 550 K and 590 K, respectively, however, at higher heating rates the rapid temperature rise may lead to an explosion at 810 K [2]. Because of the lower heating rates, DSC provides thermal information at the higher temperatures of interest after consumption of reactants, and therefore, may not be representative of the sample thermal behavior at actual process conditions. Thus, high heating rates must be used to reach higher temperatures before the occurrence of significant substance decomposition and chemical reactions. High-energy initiators produce heating rates of several tens to hundreds of degrees per second and temperatures in excess of 1300 K. The rapid attainment of high temperatures to initiate and diagnose such reactions is achievable by using laser-heating techniques.

Laser-heating techniques, in general, have become popular as diagnostics for a variety of parameters in many applications. Examples include photoacoustic spectroscopy, which has been used to measure the absorption characteristics of aerosols [3–6]. The technique uses a modulated light source to heat a substance in a resonance cavity, which in turn, transfers heat to the surrounding air. The periodic heating of the air results in the formation of periodic pressure fluctuations, creating an acoustic signal that is then detected [7]. The technique measures the integrated, line-of-sight absorption from the ensemble of particles in the cavity. Although low-power light sources are used for certain applications, pulsed Nd:YAG laser heating has been used with nanosecond pulses and thus one area of concern is the effect of the laser pulse on particle heating [4]. Several techniques exist that use high heating rates to determine substance properties. For example, two techniques are laser breakdown spectroscopy (LIBS) and laser induced incandescence (LII). In LIBS, a focused pulsed Nd:YAG laser is used to rapidly heat substances (in particular, metals) and form a high temperature microplasma (on the order of 10,000 K) [8]. During rapid cooling
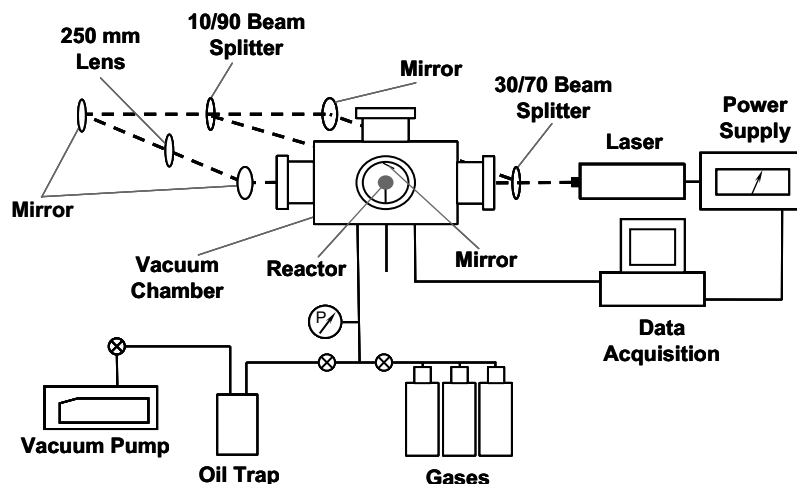
Fig. 1. Schematic of the control, optical, and gas systems of the LDTR.

of the sample, radiation is emitted and a spectrometer is used to determine the sample composition. Issues include the effect of the excessive heating on changing the substance properties [9], and plasma decay rates vary for different species so LIBS must be optimized for each species [10]. In LII, a pulsed Nd:YAG laser is used to heat particles to the carbon vaporization temperature ($\approx$4000 K) [10]. Using the thermal energy balance equation and knowledge of the temperature decay time after heating, one can determine the soot primary particle size and volume fraction [11]. Longer decay times are indicative of larger particle sizes [12]. One issue is the effect of laser heating on soot particle morphology and the size distribution [12].

Conventional thermal analysis techniques are designed to measure a selected thermal or chemical property in a nominally near steady-state thermal environment. There is no single conventional technique available that provides thermophysical properties, and information on chemical kinetic rates and reactions. This article describes the application of a thermal-heating technique, referred to as the laser-driven thermal reactor (LDTR), to different solid, liquid, and gaseous substances in oxidative and pyrolytic environments. The LDTR technique measures the total thermal response (i.e., due to both substance thermal and chemical heat release). The technique is used to provide quantitative information on thermophysical (e.g., heat capacity, thermal conductivity, emissivity, and absorptivity) and chemical processes (i.e., exothermic and endothermic reactions), sequence of reactions, and rate constants for multicomponent and multiphase substances. Recently, the technique was used to determine the absorption coefficient of carbonaceous-based substances, i.e., clean quartz filters, filters contaminated with laboratory air particles and combustion-generated soot, and disk- and sphere-shaped activated carbon pellets at different sample temperatures, inert gas environments, and gas pressures [13]. It was also found that the gas environment and pressure had negligible effect on the sample absorptivity, but substance shape and mass played an important role in determi-

nation of the absorptivity. This article presents the overall experimental and theoretical details, as well as examples that demonstrate the technique under different thermal and physical conditions.

## 2. Experimental arrangement

The laser-driven thermal reactor consists of a sphere-shaped reactor mounted within a vacuum chamber, along with integrated optical, gas supply, and computer-controlled data acquisition subsystems, see Fig. 1. At the center of the reactor, the sample material rests on a thermocouple. The reactor assembly is heated from opposing sides by an infrared laser to achieve nearly uniform sample temperature. The vacuum chamber allows for control of the environment (e.g., humidity, gas pressure, gas composition) that surrounds the sample. The change in sample and reactor temperature with time is recorded by the data acquisition system and this information is then processed for the specified thermophysical information of interest. Additional information on the substance chemistry can be obtained from extractive sampling of the reaction gases, and introduction of these gases into a gas chromatography/mass spectroscopy system.

The reactor is a small copper-foil sphere (with an outer diameter of $18.2 \pm 0.1$ mm[1] and thickness of 0.14 mm) within which a sample is placed at the sphere center, see Fig. 2. Experiments were carried out to select a reactor diameter and thickness that ensured adequate thermal conduction through the copper material and at the same time

---

[1] Estimation of the measurement uncertainty for this study is determined from statistical analysis of a series of replicated measurements (referred to a Type A evaluation of uncertainty), and from means other than statistical analysis (referred to Type B evaluation of uncertainty) [14]. The Type A uncertainty is calculated as $ku_c$, where $k$ is the coverage factor and $u_c$ is the combined standard uncertainty. The value for $u_c$ is estimated statistically by $sn^{-1/2}$, where $s$ is the standard deviation of the mean and $n$ is the number of samples. For $n = 50$, $k = 2.01$, representing a level of confidence of 95%.
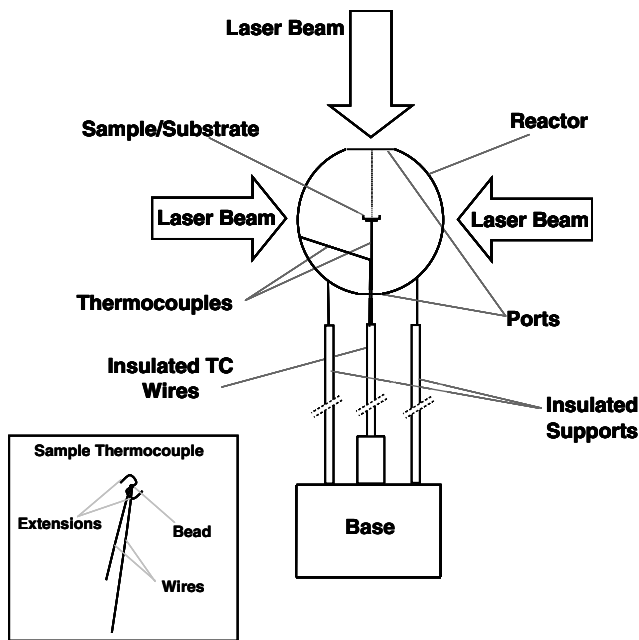
Fig. 2. Schematic of the LDTR reactor sphere. The reactor diameter is approximately 18.2 mm with an opening in the top ($\approx$7.2 mm diameter) and bottom ($\approx$4.0 mm diameter). The insert details the sample thermocouple located in the center of the reactor.

maintained the high heating rates (which would be reduced if the foil was too thick). Different material thicknesses (40–200 μm) and sphere diameters (12–25 mm) were examined by monitoring the temperature rise with time on the copper inner surface and at the center of the reactor. After softening a piece of copper, the reactor is fabricated by pressing the copper into a stainless steel ball-shaped form, which results in a hemisphere. Two pieces are made and spot-welded together. The untreated copper foil is malleable, however, after being formed into a sphere the material is fairly rigid and does not deform easily. An opening is cut in the top of the sphere (diameter of $\approx$7.2 mm) to place the sample and another opening is made in the bottom (diameter of $\approx$4.0 mm) to introduce a four-passage ceramic tube that supports the wires and exposed beads (junctions) of two thermocouples. At the center of the reactor, the sample rests on thermocouple-wire extensions (0.025 mm in diameter) protruding from near the bead of one K-type fine-wire thermocouple (0.025 mm in diameter, unsheathed), i.e., 'sample' thermocouple, see insert in Fig. 2. If needed, a disk-shaped substrate (of copper or nickel with a diameter of approximately 5 mm and thickness of 0.14 mm) is used to support the sample on the extensions. The reactor inner wall is in contact with the second thermocouple (i.e., 'reactor' thermocouple), which is bent from the central ceramic tube (i.e., through the bottom port of the reactor) to the reactor inner wall surface and is flush with the wall at a vertical distance of approximately 4.5 mm from the bottom of the sphere. The thermocouples were fabricated in-house using spot-welding technology. The bead diameter for both thermocouples was 0.025 mm. A resistively heated ceramic

tube (with a 9 mm outer diameter and 40 mm long) was fabricated to calibrate in the same environment the thermocouples against similar commercially available K-type thermocouples. The thermocouple readings were not corrected for radiation effects. The thermocouple time response was estimated to be 0.05 s to reach 63.2% of an instantaneous temperature change. The expanded uncertainty for the temperature was 7 K, including the Type B uncertainty of 3.1 K. The temperature from each thermocouple is recorded by the data acquisition system at a rate of 10 samples per second. The reactor and substrate are placed prior to use in a small nonsooting methanol flame under ambient conditions to generate a copper oxide layer, which reduces laser beam scattering effects off of their surfaces, as well as reactivity and heat transfer effects due to formation of the oxide layer during experiments.

The reactor is positioned in the center of a 5 L vacuum chamber with five viewing ports and a manually operated linear traverse to enable reactor accessibility (see Fig. 1). The top of the chamber provides access to the reactor and is sealed with an o-ring. Each viewing port includes a vacuum-sealed 76 mm diameter quartz window, which is suitable for transmission of laser beams to the reactor. The source of the laser beams is a 250 W multi-mode, continuous-wave Nd:YAG laser, operating at a wavelength of 1.064 μm. The infrared laser beam heats the reactor from opposing sides using concomitant optics to direct the beam to the reactor, as shown in Figs. 1 and 2. Digital control of the laser intensity by means of the laser arc lamp current allows for programming of the desired steady-state temperature and heating rate by the data acquisition system. Different temperature regimes can be interrogated by changing the laser fluence. Some advantages of using laser heating over other heating methods, such as electrical resistance heating, include higher heating rates, direct reactor heating to the sample to eliminate convective heating of the surrounding gases, and measurement of the total thermal loss (including both thermal and chemical contributions) with direct sample heating.

One mode of thermal analysis involves heating the reactor in this manner at two different laser fluences (referred to as the 'heating-rate' approach). Chemical kinetic parameters (i.e., endothermic and exothermic rate constants) of the chemical processes are deduced from this approach from time-resolved temperature measurements of the sample and reactor. Another mode of thermal analysis involves direct laser heating of the sample from a third diverted beam (through a chamber side port and off a mirror inside the chamber) down through the opening in the top of the reactor (see Fig. 2), which is referred to as the 'direct-heating' approach. The diverted beam power has been measured inside the vacuum chamber with a power meter to be less than 3% of the total incident power. This approach decouples experimentally the effects of chemical heat release, and convective and radiative heat losses to obtain thermophysical properties (e.g., emissivity and absorptivity). Although the two approaches are equivalent [15],

and were confirmed experimentally, there are advantages to using one approach over the other, as will be discussed.

Substances that can be analyzed include solids, liquids, and various multiphase and multicomponent inhomogeneous substances. The laser beam is expanded with a lens to about the diameter of the sphere (checked qualitatively with an infrared beam display plate) to reduce the temperature variation over the reactor surface. The thermal conductivity of the copper sphere is assumed to help smooth out effects due to non-uniformity of the multi-mode laser beam intensity. The sample is heated via radiative transport from the inside surface of the reactor sphere. The high thermal conductivity of the copper sphere, and radiation heat transfer between the interior sphere surface and the sample within the sphere, results in a nearly uniform sample temperature. This uniformity in sample temperature depends on the relative dimensions of the sample and reactor sphere, laser beam width, and reactor thermal conductivity. Measurements using a rake of commercially available fine-wire thermocouples found that the gas temperature was uniform to within the thermocouple uncertainty for a volume with dimensions of about 10 mm diameter by 5 mm height near the center of the sphere. Thus, millimeter-sized sample is kept to within these dimensions [15]. The effects of temperature on thermal conductivity and specific heat of copper (e.g., the values at 298 K and 1000 K are 4.01 W cm$^{-1}$ K$^{-1}$ and 3.52 W cm$^{-1}$ K$^{-1}$, and 0.385 J g$^{-1}$ K$^{-1}$ and 0.451 J g$^{-1}$ K$^{-1}$, respectively [16]), are taken into account when necessary. Heating rates on the order of several hundred K/s can be achieved, depending on the maximum achievable laser power and time response of the thermocouple. The apparatus can analyze (within the above-mentioned measurement volume) sample masses from a few milligrams up to a few grams. The surrounding environment can handle a variety of gas compositions (e.g., oxidizing, humid, inert, mixtures), and gas gauge pressures (ranging between 10 Pa and 505 kPa). In this study, only inert gases were used (to prevent oxidation of volatile matter and other reactions on the sample surface) for chamber gauge pressures of 5.1 kPa, 15.2 kPa, and 50.7 kPa.

As an example of the LDTR performance, we compared the time required to heat and measure the temperature of a simulant high-level organic waste (performance assessment standard PAS 94), using both the LDTR and a DSC [17,18]. The characteristic time to complete a measurement with the LDTR was 10.6 s while the DSC required 6600 s to reach 825 K, thus the LDTR heating rate was approximately 50 K/s, while that of the DSC was 0.08 K/s [18]. Also, the LDTR was able to reach a temperature of over 2000 K, which at the same heating rate took about 34.1 s. The effect of heating rate on identifying substance decomposition is exemplified in Fig. 3, which presents the temperature difference between the sample and reactor (i.e., $T$–$T_r$ where $T$ is the sample temperature and $T_r$ is the reactor temperature) with respect to time of activated carbon pellets for three different heating rates. The results indicate
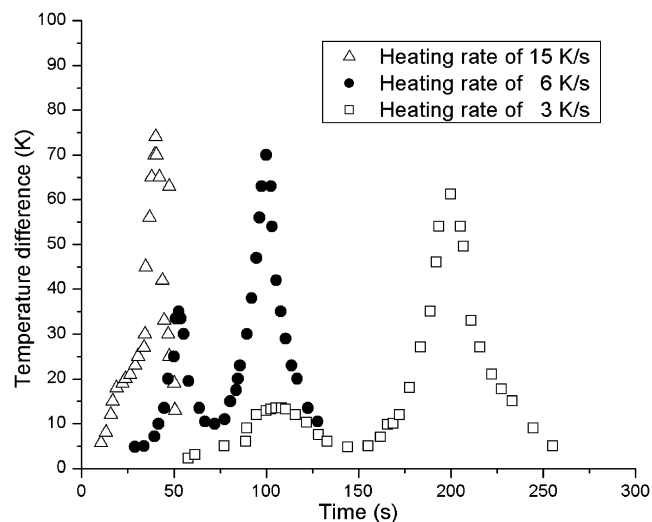


Fig. 3. Variation of the difference in temperature between the reactor and sample with time of activated carbon pellets at three different heating rates.

that as the system heats up to the operating temperature of about 400 K at 3 K/s two peaks form preferentially with time, with the earlier peak attributed to vaporization of volatile matter and the second peak attributed to decomposition of the carbon. Although not examined, the DSC would not be expected to resolve the earlier peak at the operating temperature because of its relatively low heating rate. At the higher heating rate of 15 K/s, with the sample heated to about 600 K, essentially one peak is formed, which is attributed to decomposition of all volatile components of the activated carbon at the operating temperature. Thus, this result demonstrates how the heating rate can be adjusted to reveal different thermal and chemical reaction phenomena.

## 3. Theoretical considerations

### 3.1. Thermal energy balance

The theoretical model is based on a representation of the heating process associated with the above-mentioned experimental arrangement for a given temperature and wavelength. The following thermal energy balance governs the heating process:

$$c_p m \, \mathrm{d}T/\mathrm{d}t = R_1(T_r) - R_2(T)$$
$$= IA\beta(T,\lambda) - F(T,T_0) + m_c q(T) \qquad (1)$$

where the time rate of change of internal energy is given by the term on the left side of Eq. (1), $R_1(T_r)$ is the rate at which heat is transferred from the reactor at temperature $T_r$ to the sample and substrate (corresponding to the first term on the right side of the equation), and $R_2(T)$ is the rate of heat loss from the sample and substrate (corresponding to the second and third terms on the right side of the equation), $T$ is the sample/substrate temperature, $c_p$ is the

sample specific heat, $m$ is the sample total initial mass, and $t$ is time. The sample specific heat and mass (and other temperature-dependent properties, if part of the analysis) are dependent on temperature and thus adjusted according to the experimental conditions. The change in mass during thermal heating and chemical reaction is considered and accounted for in the determination of the energy release by weighing the sample initially and after heating. The first term on the right side of Eq. (1) is the laser energy absorbed by the sample [11], where $I$ is the intensity of the laser beam that heats the sample, $A$ is the sample geometric cross-sectional area, $\beta(T, \lambda)$ is the absorptivity of the sample at temperature $T$ and laser wavelength $\lambda$. The absorptivity is defined as $\beta(T, \lambda) = \alpha d_c = 4\pi k d_c/\lambda$ [19], where $\alpha$ is the sample absorption coefficient, and $d_c$ is a characteristic path length through the sample, and $k$ is the imaginary part of the complex refractive index. The heat transfer term $F(T, T_0)$ depends on the sample shape and represents the sample thermal losses due to conduction through the gaseous medium, conduction through the temperature sensor wires, and radiation (the main mode of heat transfer). Convection is assumed to be negligible inside the reactor due to its small size and the low gas pressure, i.e., the Nusselt number will be small. The parameter $T_0$ is the sample temperature at steady-state (see Fig. 4a). Heat transfer due to chemical reaction is given by the last term of Eq. (1), and is

included if the substance is chemically reactive. The parameter $m_c$ is the mass of the reactive portion of the sample (determined by weighing the sample before and after the experiment, and assuming that only the nonreactive portion of the sample remains upon completion of the experiment), and $q(T)$ is the specific heat release rate due to chemical reaction [20].

### 3.2. Heating regimes and approaches to analysis

Eq. (1) enables prediction of the different LDTR heating regimes, as illustrated by the numbered segments of the heating curve shown in Fig. 4a, and determination of the substance thermophysical properties. The different regimes of the heating curve are represented by the (1) temperature rise (laser heating and an increase in the sample temperature), (2) steady-state (for which there is no longer a change in temperature with time), and (3) decay (for which the incident laser beam intensity is zero and the sample temperature decreases). Specifically, the three regimes (assuming no chemical reactions) can be expressed by

Temperature rise : $c_p m (\mathrm{d}T/\mathrm{d}t)_R = IA\beta(T, \lambda) - F(T, T_0)$ (2)

Steady-state : $IA\beta(T, \lambda) = F(T, T_0)$ (3)

Temperature decay : $c_p m (\mathrm{d}T/\mathrm{d}t)_D = -F(T, T_0)$ (4)

The aforementioned heating-rate approach is represented by the first two regimes (i.e., the initial temperature rise and steady-state heating, resulting from laser heating of the reactor) and is denoted by 1 in Fig. 4a. For the direct-heating approach, the initial regimes of heating are not analyzed (as given by segment 1 in Fig. 4a), but the sample is directly heated by a third beam to produce a slight rise in temperature after reaching the steady-state temperature, as indicated by segments 2 (temperature rise), 3 (steady-state), and 4 (temperature decay) in Fig. 4a. Thus, Eqs. (2)–(4) are used to describe segments 2–4 in Fig. 4a, respectively.

These two approaches have been shown to produce equivalent results [15] and thus provide a means of system self-validation. This self-validation is carried out by determining $F(T, T_0)$ as given by Eq. (4), which can be rewritten after separation of variables and integration to have an exponential form [21]. Thus, for an exponentially decaying function, the sample temperature is given by

$$T - T_0 = (T_{max} - T_0)\mathrm{e}^{(-t/\tau)} \quad (5)$$

where $T_{max}$ and $T_0$ are the steady-state sample temperatures defined in Fig. 4a, and $\tau$ is the temperature-dependent relaxation time. Taking the derivative of Eq. (5) with respect to time, it can be shown that

$$\mathrm{d}T/\mathrm{d}t = -(T - T_0)/\tau \quad (6)$$

and

$$F(T, T_0) = \gamma(T - T_0) \quad (7)$$

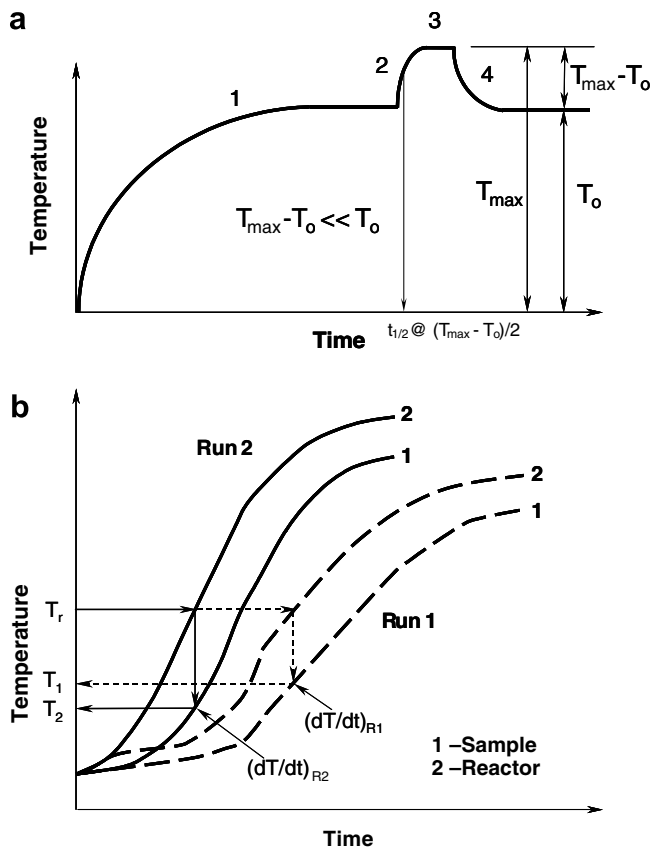

Fig. 4. Schematic of the thermal analysis process for the LDTR (a) direct-heating and (b) heating-rate approaches.

where $\gamma \equiv c_p m/\tau$. For the heating-rate approach, an analytical expression can be derived for $\tau$ knowing that for a constant reactor temperature, the sample temperature will vary according to Eq. (6), viz.,

*Heating-rate approach*:

$$\tau(T) = \frac{T_2 - T_1}{\left(\frac{dT}{dt}\right)_1 - \left(\frac{dT}{dt}\right)_2} \tag{8}$$

where $T_1$ and $T_2$ are the sample temperatures at time $t$ for the two different laser fluences. For the direct-heating approach, an analytical expression can be derived for $\tau$ knowing that for a constant reactor temperature, the sample temperature will vary according to Eq. (5), viz.,

*Direct-heating approach*:

$$\tau(T) = \frac{t}{\ln\frac{T_{max} - T_0}{T - T_0}} \tag{9}$$

Thus, the heat transfer parameter $\gamma$ should be the same at a given sample steady-state temperature regardless of the measurement approach. A comparison of results using both approaches is presented in Fig. 5, which presents the variation of the inverse relaxation time with sample temperature for both heating approaches using nitromethane. A linear fit through the data is also presented for the direct-heating approach. The figure indicates that the data for both approaches agree to within 15% of the linear fit.

By varying the operating condition of the LDTR, one can reformulate Eqs. (2)–(4) to provide accurate determination of different thermophysical properties. As an example, the heating-rate approach can be used to determine substance reactivity by measuring the total energy released during heating of the substance at different laser fluences. The analysis is based on solving Eq. (2) for $F(T, T_0)$ along with determining the sample temperature and rate of temperature change at two different heating rates. To determine the sample temperature obtained at the two different heating rates, the reactor temperature must remain unchanged. To accomplish this, a reactor temperature ($T_r$) is chosen and the sample temperatures ($T_1$ and $T_2$), as well as the corresponding sample temperature derivatives $(dT/dt)_{R1}$ and $(dT/dt)_{R2}$, are obtained by extrapolation to the appropriate curves, as illustrated in Fig. 4b. For example, the sample and reactor temperatures are recorded for two runs at two different laser fluences, and a common value of $T_r$ is chosen for which there is sufficient sensitivity to determine the above-mentioned derivatives. For the first run and chosen value of $T_r$, the sample temperature $T_1$ and derivative $(dT/dt)_{R1}$ are determined that corresponds to the same time when the chosen value of $T_r$ was attained during the run. The sample temperature $T_2$ and derivative $(dT/dt)_{R2}$ for the second run are then determined for the chosen value of $T_r$ in a similar manner as for the first run.

An example of the use of the direct-heating approach (see Fig. 4a) and manipulation of the aforementioned thermal balance equations for absorptivity, $\beta(T, \lambda)$, is to first determine the internal energy rate term on the left side of Eq. (2) by using the measured heating rate during the temperature rise, $(dT/dt)_R$. The mass of the sample is measured with a precision balance prior to placement on the reactor substrate (and checked again after the measurement to look for any appreciable change in mass). The term $F(T, T_0)$ in Eq. (4) is then determined by using the measured heating rate during the temperature decay, $(dT/dt)_D$. When the sample heating rate is negligible during the laser pulse (i.e., at the steady-state temperature), it then follows that $\beta(T, \lambda)$ at the laser wavelength can be determined by measuring the steady-state temperature at the specified illumination power (see Eq. (3)). This procedure can be repeated at different laser fluences. Eq. (2) can then be used to check for consistency. As stated earlier, it follows that the absorption coefficient can be determined once $\beta(T, \lambda)$ is known.

## 4. Results and discussion

To demonstrate the application of the LDTR, experiments were carried out with a simulant hazardous organic waste PAS 94 [1], and nitromethane. Heating rates were measured for different substances, and chemical kinetics information was obtained at various temperatures and heating rates. Analyses were carried out to better understand processes associated with the substance thermal behavior, i.e., exothermic and endothermic, for which the endothermic behavior could be attributed to water vaporization, melting, and/or thermal decomposition. These studies demonstrate the variety of substances that may be analyzed and the importance of detecting accelerated rates of heat release that may lead to uncontrolled chemical reactions.
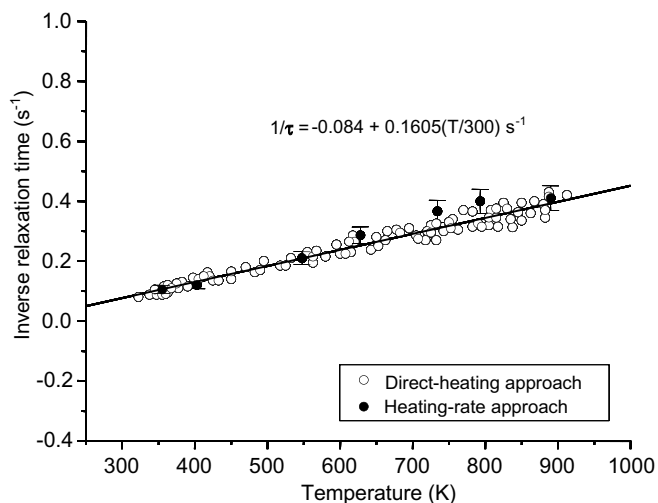


Fig. 5. Variation of inverse relaxation time with sample temperature for both heating approaches using nitromethane.

## 4.1. Simulant high-level organic waste PAS 94

The total heating value and heat release rate of waste exothermal processes can act as a means to characterize the tendency for uncontrolled reactions (e.g., thermally explosive reactions). As an example, the LDTR and a DSC (at heat rates up to 5 K/min) were used to study the behavior of PAS 94, a simulant organic solid waste [17,18]. This simulant consisted of over 24 different compounds including organics, solvents, sodium nitrate, sodium nitrite, additives, and inorganics, see Table 1. There was no appreciable mass change in the PAS 94 sample during the experiments. Results were compared between untreated waste and sample pre-dried in a vacuum oven at room temperature for two days. LDTR measurements were carried out at different heating rates and steady-state sample temperatures. DSC results with untreated sample (see Fig. 6a) indicated that at temperatures between 300 K and 450 K there was a strong endotherm of about 731 J/g, and an exotherm at 500–650 K of about 654 J/g; the net energy absorbed was 71 J/g (the dashed lines represent the peak/valley baseline). At a temperature of 730–780 K, the instrument detected an exotherm of about 5.8 J/g. The results with sample pre-drying (see Fig. 6b) caused the exothermal energy release at 500–650 K to decrease from 654 J/g to 359 J/g. The endotherm at 300–450 K decreased significantly from 731 J/g to 76 J/g and the exotherm at 730–780 K increased from 5.8 J/g to

Table 1
Chemical composition of the simulant organic waste PAS 94

| No. | Compound | Percent weight |
|-----|----------|---------------|
| 1 | NaOH | 31.48 |
| 2 | $NaNO_2$ | 7.39 |
| 3 | $NaC_2H_3O_3$ sodium glycolate | 7.10 |
| 4 | Na3HEDTA | 5.57 |
| 5 | Na4EDTA | 3.41 |
| 6 | Na3citrate · $H_2O$ | 1.94 |
| 7 | $Na_2C_4H_4O_6$ · $H_2O$ sodium tartrate | 0.54 |
| 8 | Na D2EHP | 0.70 |
| 9 | Tributyl phosphate | 0.35 |
| 10 | NPH ($C_{12}H_{26}$) | 3.75 |
| 11 | $Fe(NO_3)_3$ · $6H_2O$ | 4.58 |
| 12 | $Cr(NO_3)_2$ · $9H_2O$ | 0.08 |
| 13 | $Ni(NO_3)_2$ · $6H_2O$ | 0.12 |
| 14 | $Ca(NO_3)_2$ · $H_2O$ | 0.22 |
| 15 | $Mn(NO_3)_2$ | 0.05 |
| 16 | $Na_2SiO_3$ · $9H_2O$ | 0.14 |
| 17 | $NaNO_3$ | 15.40 |
| 18 | $Pb(NO_3)_2$ | 0.41 |
| 19 | Zr(citrate) | 0.01 |
| 20 | $Na_2SO_4$ | 8.72 |
| 21 | $Na_3PO_4$ · $12H_2O$ | 0.48 |
| 22 | $NaAlO_2$ · $0.21NaOH$ · $1.33H_2O$ | 1.24 |
| 23 | NaF | 0.00 |
| 24 | $H_2O$ | 6.30 |
| Total | | 100.00 |

PAS – performance assessment standard; HEDTA – hydroxyethyl ethylenediamine triacetic acid; EDTA – ethylenediamine tetraacetic acid; D2EHP – di-2-ethylhexyl phthalate; NPH – normal paraffin hydrocarbon.
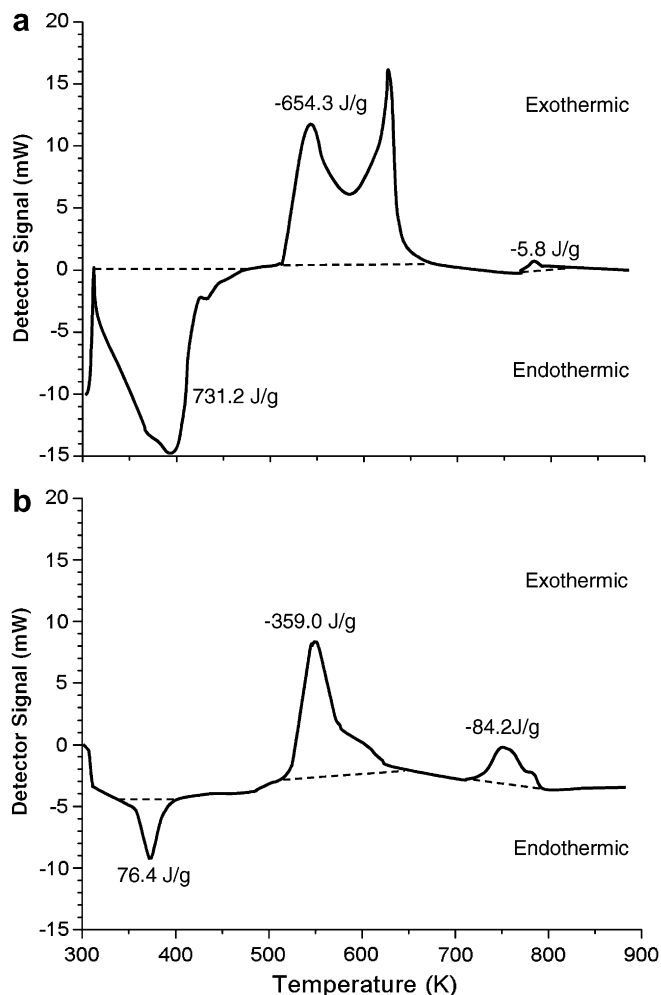


Fig. 6. Thermal-heating process by the differential scanning calorimeter for the (a) untreated and (b) pre-dried simulant waste PAS 94. The dashed lines represent the peak/valley baseline.

84 J/g. As a result, the net energy release increased to 367 J/g, which was attributed to a decrease in evaporation of water.

Using the heating-rate approach, the variation of sample temperature with time without and with pre-drying of the PAS 94 waste are presented in Fig. 7a and b, respectively. The figure presents heating curves for both the baseline (i.e., heating of the substrate without sample) and sample (i.e., sample with the substrate). The arrows indicate the presence of an accelerated rate of heat release at about 25 s. The dashed line is a curve fit to the data prior to the accelerated heat release at 25 s to indicate how the data might evolve at higher sample temperatures if the process remained endothermic. The energy released (exothermic) or absorbed (endothermic) by the sample with time is function of the temperature difference between the sample and baseline, as presented in Fig. 8 for the untreated and pre-dried simulant waste PAS 94, respectively. One can solve Eq. (1) using the temperature difference given in Fig. 8 to obtain the specific heat release rate due to chemical reaction, $q(T)$ (with $q(T) < 0$ representing an endotherm and $q(T) > 0$ representing an exotherm).
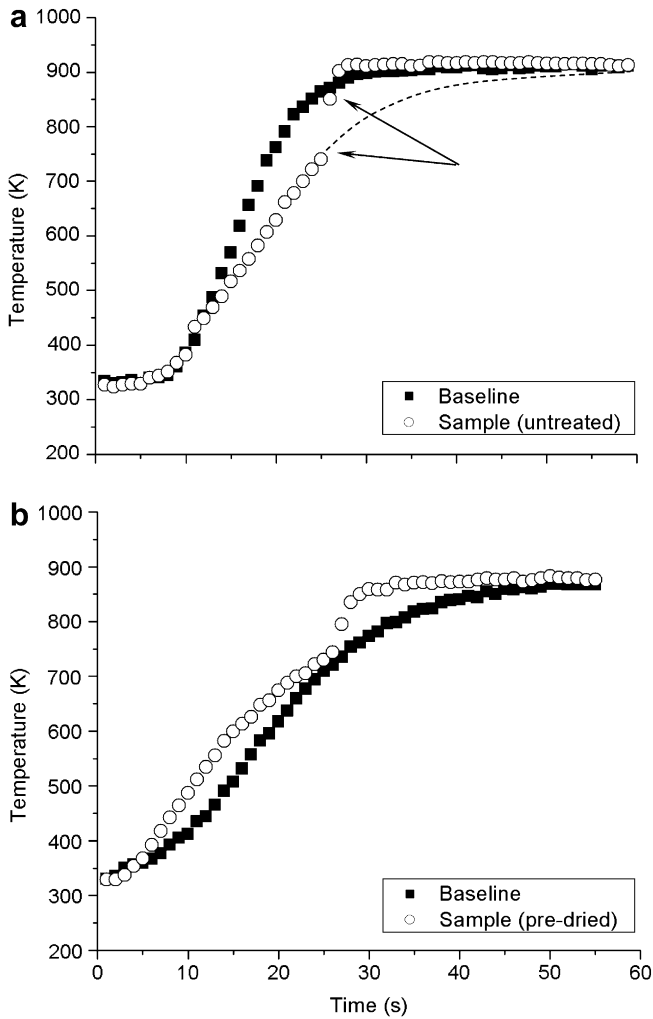
Fig. 7. Variation of the sample temperature with time for the (a) untreated and (b) pre-dried simulant waste PAS 94. Measurements for the untreated waste (mass of 14 mg) were carried out in air at 101.3 kPa, and the pre-dried waste (mass of 14.6 mg) was in argon at 8.1 kPa. The arrows indicate the presence of an accelerated rate of heat release. The dashed line is a curve fit to indicate how the data might evolve if the process remained endothermic.
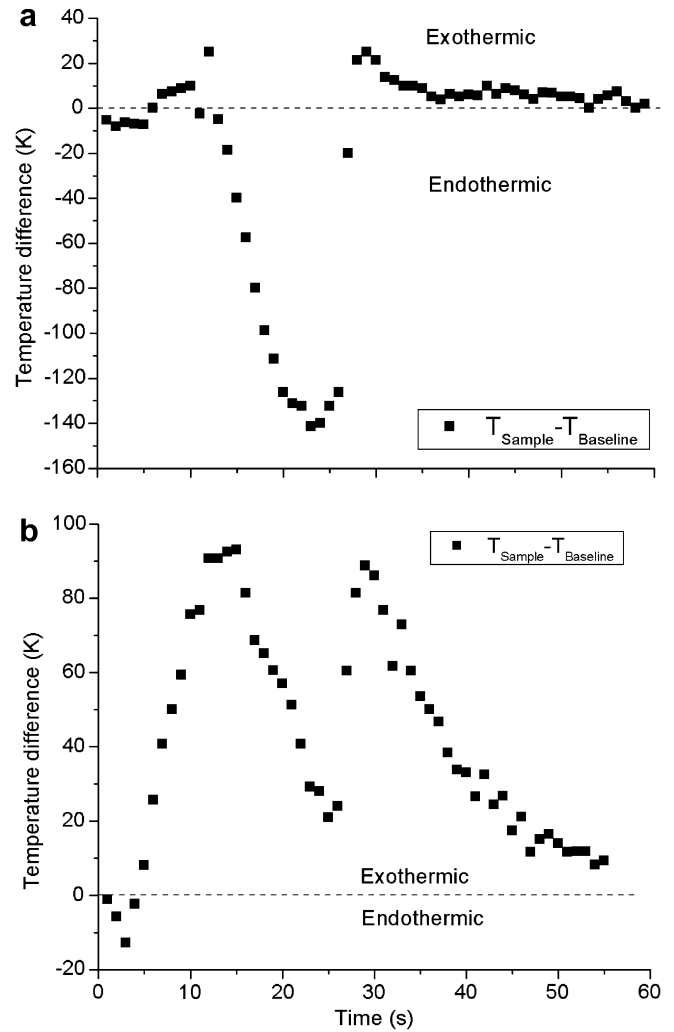


Fig. 8. Variation of the temperature difference between the sample and baseline with time for the (a) untreated and (b) pre-dried simulant waste PAS 94.

Comparing the results in Fig. 8 with Fig. 7, one can deduce for the untreated waste that the process was endothermic between 440 K and 735 K and exothermic between 735 K and 910 K, while for the pre-dried sample the process was exothermic between 350 K and 880 K. Fig. 9 presents the variation in specific heat release rate with respect to sample temperature for (a) endothermic (for the untreated waste between 440 K and 630 K), (b) exothermic (for the pre-dried waste between 375 K and 500 K), and (c) exothermic processes (for both the untreated and pre-dried wastes between 735 K and 910 K), respectively. Note that the ordinate is presented as a natural (base $e$) logarithmic scale. The chamber pressure was set at 101 kPa in air for the untreated waste, and at 8.1 kPa in argon for the pre-dried waste. Note that thermal convection was found to be independent of the pressure up to 150 kPa [15], thus the different chamber pressures were assumed to have negligible effect on the results. The sample specific heat release

rate (for both endothermic and exothermic processes) is assumed to be represented by the following Arrhenius-type expression:

$$q(T) = q_0 \exp(-E/T) \tag{10}$$

where $q_0$ is a pre-exponential coefficient, and $E$ is an exponential coefficient in units of absolute temperature. The time integral of the differential specific heat release rate, which provides the total specific heat release (or absorption), is then expressed by

$$Q = \int q(T)\,\mathrm{d}t. \tag{11}$$

One can determine the values of the co-efficients by curve fitting the data presented in Fig. 9 using Eq. (10), and the results are presented in Fig. 9. The sample thermal behavior can then be described by applying Eqs. (10) and (11) to the above-mentioned temperature regimes of the thermal heating process.

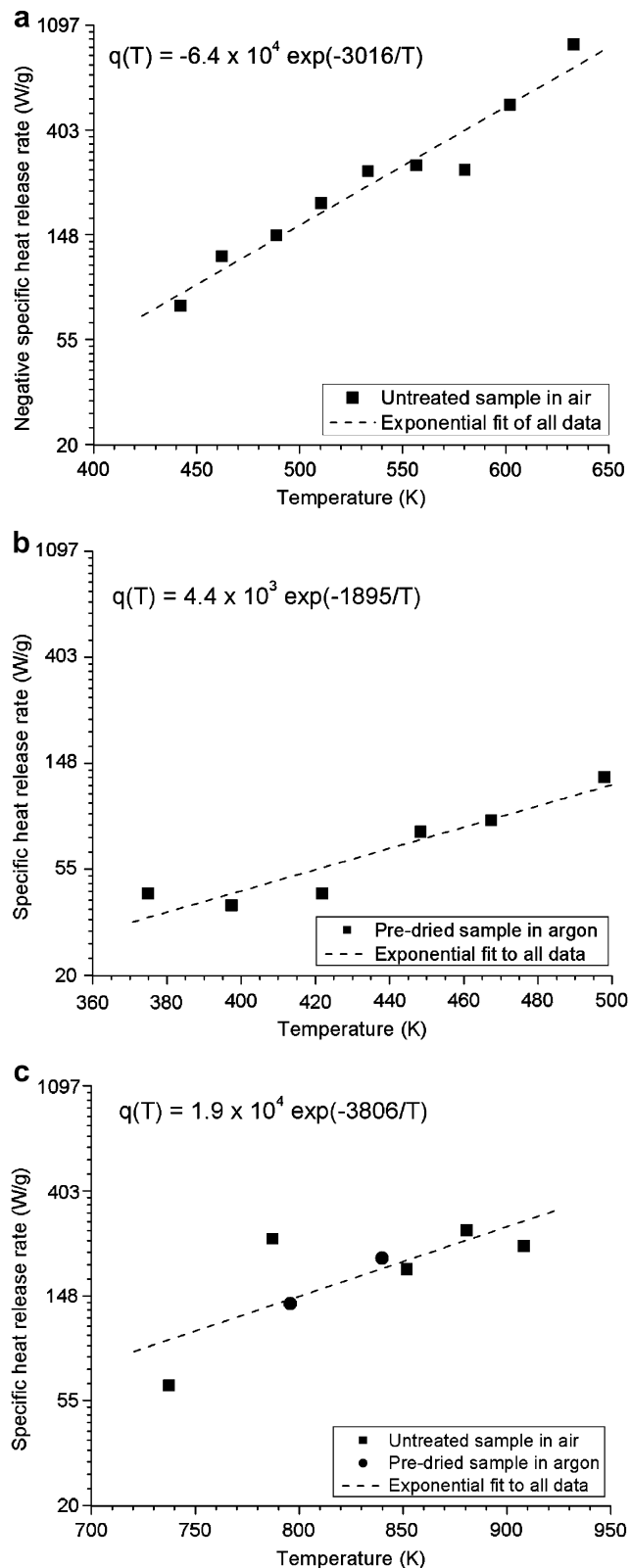The results for the untreated sample indicate that endothermic processes dominate in the early stage of heating,

**a**

$$q(T) = -6.4 \times 10^4 \exp(-3016/T)$$

- ■ Untreated sample in air
- - - - Exponential fit of all data

*Negative specific heat release rate (W/g)* vs *Temperature (K)*

**b**

$$q(T) = 4.4 \times 10^3 \exp(-1895/T)$$

- ■ Pre-dried sample in argon
- - - - Exponential fit to all data

*Specific heat release rate (W/g)* vs *Temperature (K)*

**c**

$$q(T) = 1.9 \times 10^4 \exp(-3806/T)$$

- ■ Untreated sample in air
- ● Pre-dried sample in argon
- - - - Exponential fit to all data

*Specific heat release rate (W/g)* vs *Temperature (K)*

Fig. 9. Variation of the specific heat release rate with sample temperature for (a) lower temperature results obtained from the untreated sample, (b) lower temperature results obtained from the pre-dried sample, and (c) higher temperature results from both the untreated and pre-dried PAS 94 simulant waste. Note that the ordinate is presented as a natural (base *e*) logarithmic scale. Also, the ordinate of Fig. 9a is the negative of that for Fig. 9b and c.

i.e., in the sample temperature range of 440–630 K (where the heating curve for the sample is below the baseline in Fig. 7a), and exothermic processes dominate in the sample temperature range of 735–910 K (where the heating curve is above the baseline in Fig. 7a and b) [17,18]. Presumably, the accelerated rate of heat release at 25 s (see Fig. 7a) is attributed to completion of the endothermic process and initiation of the exothermic process. Thus, assuming a two-stage process, one finds that for the untreated sample, the total endothermic specific heat release for the lower temperature range (defined as Stage A, see Fig. 9a) was −1.2 kJ/g. The total exothermic specific heat release for the higher temperature range (defined as Stage B, see Fig. 9c) was 2.9 kJ/g. The total heating value of the untreated sample (i.e., endotherm and exotherm together) was 1.7 kJ/g. In the case of the pre-dried sample, heating was exothermic and not endothermic at the lower sample temperatures (from 375 K to 500 K). For this Stage A, the total exothermic specific heat release was 0.6 kJ/g, and for Stage B the exothermic heat release was 1.2 kJ/g. The total heating value of the pre-dried sample was 1.8 kJ/g. Although the reaction characteristics of these two exothermal processes are different, as substantiated by the different thermal behavior for the untreated and pre-dried samples, the overall kinetics (i.e., thermal energy release) appear to be similar. These results were verified in both oxidizing (air) and in inert gas (argon) environments. These results suggest that the thermal release characteristics of PAS 94 waste may not depend on combustion of organics in oxygen.

As mentioned earlier, sodium nitrite (with a melting point of 557 K [16]) and sodium nitrate (melting point of 580 K) are significant components of the PAS 94 waste (having a combined mixture weight of 22.8% of the total waste, see Table 1). Thus, the thermal behavior was also determined for these two compounds using both a DSC and the LDTR (data for both not presented for brevity). The DSC (with a heating rate of 5 K/min) results for sodium nitrite indicated the presence of a relatively small endotherm at approximately 450 K, which was attributed to melting of sodium nitrite, and another stronger endotherm between 550 K and 600 K, which was attributed to thermal decomposition. Measurements with the LDTR were carried out in argon and air at 101 kPa at heating rates between 30 K/s and 40 K/s. The results indicated the presence of an endotherm at 350 K (attributed to water vaporization) and a stronger endotherm at 550–650 K (attributed to melting and thermal decomposition of sodium nitrite), with $Q = -1325$ J/g. The latter endotherm had a linear relationship for the specific heat release rate of $q(T) = (1087 \pm 171) - (2.1 \pm 0.3)T$. An exothermic behavior was present at 650–750 K. The behavior for sodium nitrate was slightly exothermic at 400–650 K, and endothermic at 750–1000 K. The endotherm also had a linear relationship for the specific heat release rate of $q(T) = (832 \pm 79) - (1.2 \pm 0.1)T$. One possible explanation for the specific heat release rate being linear for sodium

nitrite and sodium nitrate, as opposed to the exponential relationship for the PAS 94 waste may be that the PAS 94 waste is preferentially decomposed due to the large number of components in the mixture.

## 4.2. Nitro-compounds in activated carbon

The thermal decomposition was investigated for activated carbon (AC) doped with drops of liquid nitromethane (assayed at 99.4%) and compared with data obtained for nitrobenzene- and nitrocumene-doped AC from another study [22–24]. The AC was weighed before being doped with the nitro-compound and after in order to monitor the change in mass. LDTR temperature profiles are presented in Fig. 10 for three different laser fluences. The dashed and solid curves correspond to the activated carbon without nitromethane (baseline case), and with nitromethane, respectively. The average heating rate in Run A, was 7 K/s and in Run C was 50 K/s. The thermal decomposition of nitromethane-doped AC was quicker (by a factor of about 3) for Run C than for Run A because of the quicker temperature rise during the exothermal process. During each run, the mass of the nitro-compounds was completely consumed while little change was noted in the activated carbon mass.

Following the aforementioned analysis for determining the sample specific heat release rate (see Eq. (10)), one can derive an expression (as provided in Fig. 11) for $q(T)$ for the sample temperature range of 400 K $\leqslant T \leqslant$ 950 K. Again, the ordinate in Fig. 11 is given as a natural logarithmic scale so as to simplify the determination of the coefficients in Eq. (10). An exponential fit is also presented through the data for the current experiment results. The figure indicates that the data for Run A (from Ref. [15]) and current experiment (Runs B and C) agree to within 33% of the fit (the data for the current experiment agree within 26%). Taking into account the variation of the mass
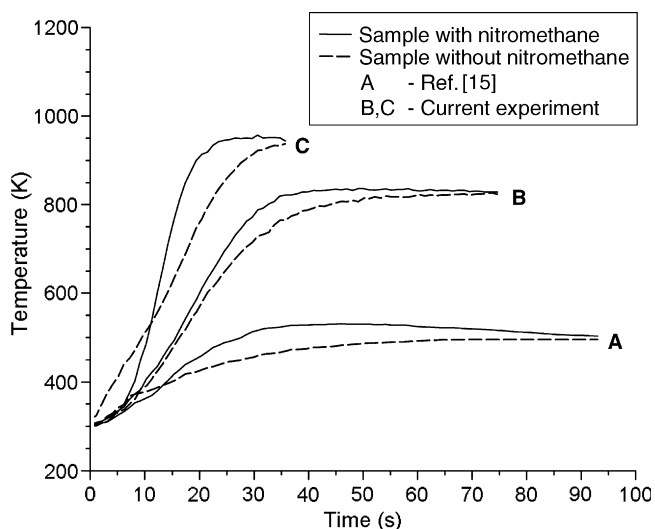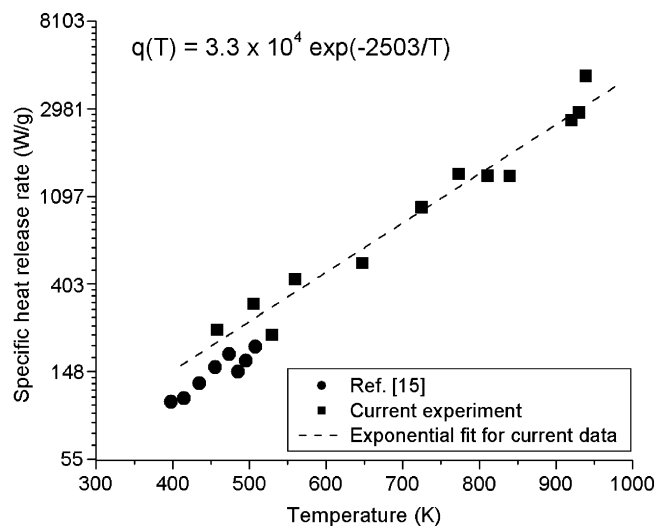


Fig. 11. Variation of the specific heat release rate with sample temperature for nitromethane. Note that the ordinate is presented as a natural (base $e$) logarithmic scale.

of nitromethane, the total specific heat release of the decomposed nitromethane-doped AC was $Q = 6.0 \pm 0.5$ kJ/g ($Q = 6.1 \pm 1.0$ kJ/g was obtained from an earlier study [15,25]). One can then determine the energy released from the dissociation of nitromethane using the change in enthalpies ($\Delta H$) available in the literature [26] for various possible reaction mechanisms, as summarized in Table 2. A comparison of the literature values (by calculating $Q$ from $\Delta H$ and species molecular weights) with measurements of the total specific heat release indicated that the third and fifth listed mechanisms had values of $Q$ closest to the measured values and therefore were considered the most likely processes. Comparison of the common byproducts between these two processes indicated that heat released in the decomposition of nitromethane was associated partially with the formation of carbon dioxide, as well as water and nitrogen.

For these experiments, the amount of absorbed nitromethane varied from 0.05 kg to 0.2 kg nitromethane per kg of carbon. Prior to the experiments, the samples were placed in the LDTR chamber containing a nitrogen atmosphere at a pressure of 5 kPa for 3–4 min in order to minimize evaporation effects. To account for this effect on the initial mass, a series of experiments were carried out to calibrate the temporal change in mass of nitromethane-doped AC at different pressures and temperatures of the surrounding environment. Similar experiments were also conducted with nitrobenzene- and nitrocumene-doped AC. The characteristic sample temperatures and the heating times were negligibly different for the three multiphase substances. A decomposition rate constant for each substance was determined using the Arrhenius expression $k_a = k_0 \exp(-E_a/RT)$, where $k_0$ is a pre-exponential coefficient, and $E_a$ is the activation energy, and $R$ is the universal gas constant (8.314 J K$^{-1}$ mol$^{-1}$), for which values are presented in Table 3. Also presented in Table 3 is the total



Fig. 10. Variation of sample temperature with time for nitromethane for three different heating rates.

Table 2
Thermodynamics of the thermal decay of nitromethane ($CH_3NO_2$): $Q$ is the total specific heat release

| Possible reaction mechanisms | $(Q_{Calculated})$ (kJ/g) | $Q_{Measured}$ (kJ/g) |
|---|---|---|
| $CH_3NO_2 \Rightarrow CO_2 + \frac{3}{5}H_2 + \frac{1}{2}N_2$ | 4.6 | $6.0 \pm 0.5$ |
| $CH_3NO_2 \Rightarrow CO + H_2O + \frac{1}{4}H_2 + \frac{1}{2}N_2$ | 3.7 | $(6.1 \pm 1.0^a)$ |
| $CH_3NO_2 \Rightarrow \frac{1}{4}CO_2 + \frac{3}{4}C + \frac{3}{2}H_2O + \frac{1}{2}N_2$ | 5.7 | |
| $CH_3NO_2 \Rightarrow \frac{1}{2}CO + \frac{1}{2}C + \frac{3}{2}H_2O + \frac{1}{2}N_2$ | 5.2 | |
| $CH_3NO_2 \Rightarrow \frac{5}{8}CO_2 + \frac{3}{4}H_2O + \frac{3}{8}CH_4 + \frac{1}{2}N_2$ | 5.6 | |
| $CH_3NO_2 + \frac{1}{4}C \Rightarrow 2CO + \frac{3}{4}CH_4 + \frac{1}{2}N_2$ | 2.7 | |
| $CH_3NO_2 + 2C \Rightarrow \frac{1}{2}C_2H_6 + 2CO + \frac{1}{2}N_2$ | 2.4 | |

 [a] Results from an earlier study [15,25].

specific heat release measured during decomposition of each substance [17]. Because of the relatively low process temperatures and that the experiments were performed in inert gas media, the decomposition of activated carbon was considered to be negligible. Dissociation of between the nitro and methyl groups during nitromethane decomposition appeared to contribute to the total released energy, since the value of $Q$ in Table 3 for nitromethane-doped AC is approximately three times larger than for nitrobenzene- and nitrocumene-doped AC. The decomposition rate constant and total specific heat release were similar for both nitrobenzene- and nitrocumene-doped AC (to within the uncertainty of the experiment) over the investigated temperature range. Thus, the decomposition mechanism was similar for these two nitro-compounds. Evidently, dissociation is controlled by the bond between the nitro group and benzene ring (see Table 3). The existence of the $(CH_3)_2CH$ group in nitrocumene did not appear to manifest itself in the chemical process.

### 4.3. Thermophysical parameters of solids

Determination of a substance thermophysical properties such as sample specific heat, $c_p$, thermal conductivity, $\kappa(T)$, absorptivity, $\beta(T)$, and emissivity, $\varepsilon(T)$ [15,24] can be accomplished for different substances by the direct-heating

approach and solving Eqs. (2)–(4) along with the sample thermal diffusivity, $\alpha_d(T)$:

$$\alpha_d(T) \equiv \kappa(T)/(\rho c_p) = Cx^2/(\pi^2 t_{1/2}) \tag{12}$$

where $\rho$ is the sample density. The term on the right is derived from the definition of the Fourier number [21,27] where $x$ is the sample thickness, $C$ is a calibration constant (usually in the range of 1.0–1.5), and $t_{1/2}$ is the time for the temperature to rise to half of its maximum value, i.e., the time associated with $(T_{max} - T_0)/2$, see Fig. 4a. For solids, the term $F(T, T_0)$ can be rewritten using Eq. (4) as an analytical expression, such as that derived for disk-shaped samples [15,24]:
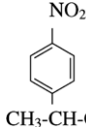
$$F(T, T_0) = c_p m \frac{(T - T_0)}{\tau} = q_c + q_r + q_{tc}$$
$$= \frac{\pi d^2}{2} \left[ 8 \frac{\kappa_g(T_g)(T - T_g)}{d(1 - \frac{d}{\pi \ell})} + \varepsilon(\lambda, T)\sigma(T^4 - T_g^4) \right] + q_{tc} \tag{13a}$$

or sphere-shaped samples:

$$F(T, T_0) = \pi d^2 \left[ 2 \frac{\kappa_g(T_g)(T - T_g)}{d} + \varepsilon(\lambda, T)\sigma(T^4 - T_g^4) \right] + q_{tc} \tag{13b}$$

where $d$ is the sample diameter, $\kappa_g(T_g)$ is the gas thermal conductivity, $T_g$ is the gas temperature, $\ell$ is the characteristic distance of the thermal loss from the sample surface, $\varepsilon(\lambda, T)$ is the emissivity, and $\sigma$ is the Stefan–Boltzmann constant ($5.67 \times 10^{-8} W \cdot m^{-2} \cdot K^{-4}$). The first term on the right hand side of the equation represents the sample thermal loss by conduction ($q_c$) through the gaseous medium (using Fourier's rate equation), the second term describes the thermal loss by radiation ($q_r$), and the third term ($q_{tc}$) is the conductive thermal loss through the thermocouple wire and radiative losses through the openings in the reactor. An estimate of the value of the last term is of the order 1–2% of the total thermal loss [15]. Eq. (13) is derived knowing the sample surface area for the particular shape,

Table 3
Parameters for determining the decomposition rate constant of activated carbon (AC) doped with different nitro-compounds

| Composition (nitro-compound doped AC) | Formula | Structure | $k_0 \times 10^{-23}$ ($m^3$/s) | $E_a/R$ (K) | $T$ (K) | $k_a \times 10^{-18}$ @$T = 400$ K ($m^3$/s) | $Q_{Measured}$ (kJ/g) |
|---|---|---|---|---|---|---|---|
| Nitromethane | $CH_3NO_2$ | $CH_3$–$NO_2$ | $2.5 \pm 1.2$ | $4800 \pm 500$ | 350 to 525 | 1.5 | $6.0 \pm 0.5$ |
| Nitrobenzene | $C_6H_5NO_2$ | NO₂ (benzene ring) | $7.0 \pm 3.0$ | $4700 \pm 400$ | 370 to 520 | 5.5 | $2.3 \pm 0.3$ |
| Nitrocumene | $C_8H_{11}NO_2$ | NO₂ (benzene ring) $CH_3$-CH-$CH_3$ | $1.1 \pm 0.2$ | $4000 \pm 300$ | 370 to 520 | 5.0 | $2.1 \pm 0.4$ |

$k_0$ is the pre-exponential coefficient, $E_a$ is the activation energy, $R$ is the universal gas constant, and $T$ is the absolute temperature for the Arrhenius expression.
Averaging was carried out for all of the experimental data [15,25].

Table 4
Total and spectral emissivity (at $\lambda = 1.06 \, \mu m$) for copper oxide (CuO) and activated carbon

| $T$ (K) | $c_p$ (CuO) ($J \, g^{-1} \, K^{-1}$) | $c_p$ (carbon) ($J \, g^{-1} \, K^{-1}$) | $\varepsilon(\lambda, T)$ | | $\beta = \varepsilon(T)$ (for $\lambda = 1.06 \, \mu m$) | |
|---|---|---|---|---|---|---|
| | | | CuO | Carbon | CuO | Carbon |
| 400 | 0.588 | 0.983 | 0.31 | 0.73 | 0.45 | 0.51 |
| 700 | 0.649 | 1.578 | 0.31 | 0.80 | 0.45 | 0.54 |
| 1000 | 0.660 | 1.962 | 0.34 | 0.80 | 0.49 | 0.59 |
| 1300 | 0.662 | 2.210 | 0.34 | – | 0.50 | – |

and integration of the general steady-state heat conduction equation with the appropriate boundary conditions [28]. Experiments were carried out to determine the thermal conduction through the surrounding medium (i.e., evaluating the first term of Eq. (13a)) with the aforementioned disk-shaped substrate for variety of chamber gases and pressures (results not reported). At a given chamber gas pressure, the thermal loss by conduction was found to increase by a factor of 25–30 when the chamber gas was changed from Xe to He. On the other hand, the thermal loss by conduction was nearly eliminated when working under vacuum (i.e., at 1 kPa).

Sample absorptivity, which is equivalent to the spectral emissivity when the substance is in an enclosure and in thermal equilibrium at the laser wavelength [19], was determined using the direct-heating method during steady-state heating (i.e., Eq. (3) is solved for $\beta$ at the laser wavelength of 1.06 μm) for a disk-shaped copper oxide substrate without sample and for disk-shaped activated carbon pellets (sieve sizes between 1.4 mm and 3.4 mm) at different sample temperatures. There was no appreciable mass change in the CuO or activated carbon during the experiments. The total hemispherical emissivity was determined during the temperature decay (see Eq. (4)) without laser heating, and using Eq. (13a). Table 4 presents the total and spectral emissivity at different sample temperatures for both of these substances [29]. No assumptions regarding the spectral nature of the substance emissivity were made (i.e., black body, gray body or non-gray body). The expanded uncertainty was estimated to be 10–15%. The temperature limit for these experiments was influenced by the melting temperature of CuO, and by the thermal decomposition of organic substances within the activated carbon. The specific heat of copper oxide and graphitic carbon [16] at the steady-state sample temperature are also listed in Table 4. The results indicated that the total emissivity was significantly different for the two samples, while the spectral emissivity was similar at lower sample temperatures but the difference grew as sample temperature increased. Jones et al. [30] carried out spectral-directional emittance measurements for copper oxide flat polished plates using a radiometric, direct-emission measurement method. The measurements were carried out over different polar angles (0–84° from the surface normal), wavelengths (1.5–8 μm), and surface temperatures (673–973 K). Comparing results for the spectral emissivity of CuO, our results appear to be somewhat lower at emission normal to the surface; however, the results are in better agreement when a different polar angle is considered.

## 5. Summary

The experimental arrangement, operation, and supporting theory were presented for a laser-driven thermal reactor that can provide temporally resolved information on substance thermophysical and chemical behavior. The technique can provide information on substance decomposition, explosion potential, thermophysical properties, chemical kinetics, and chemical reaction byproducts. Examples of the operation of the LDTR were given for simulant organic chemical waste PAS 94, nitromethane, and activated carbon to demonstrate some of the technique capabilities. Results for the specific heat release rate of the simulant organic waste PAS 94 showed that the decomposition was composed of both an initial endothermic stage followed by an exothermic stage. Results for nitromethane-doped activated carbon indicated that its decomposition is associated partially with the formation of carbon dioxide, water, and nitrogen. Results for the emissivity of copper oxide and activated carbon were compared and were similar for lower sample temperatures at the laser wavelength.

## Acknowledgements

## References

[1] R.D. Scheele, R.L. Sell, J.L. Sobolik, L.L. Burger, Organic tank safety project: preliminary results of energetics and thermal behavior, Studies of Model Organic Nitrate and/or Nitrite Mixture and Simulated Organic Waste, PNL-10213/UC-721, August 1995.

[2] R.G. Lewis (Ed.), Hawley's Condensed Chemical Dictionary, 1993, p. 1063.

[3] W.P. Arnott, H. Moosmüller, C.F. Rogers, et al., Photoacoustic spectrometer for measuring light absorption by aerosol: instrument description, Atmos. Environ. 33 (1999) 2845–2852.

[4] W.P. Arnott, H. Moosmüller, P.J. Sheridan, J.A. Ogren, R. Raspet, W.V. Slaton, J.L. Hand, S.M. Kreidenweis, J.L. Collett Jr., Photoacoustic and filter-based ambient aerosol light absorption

measurements: instrument comparisons and the role of relative humidity, J. Geophys. Res. 108 (D1) (2003) 4034–4044.

[5] L. Krämer, Z. Bozoki, R. Niessner, Characterisation of a mobile photoacoustic sensor for atmospheric black carbon monitoring, Anal. Sci. 17 (2001) 563–566.

[6] A.B. Tikhomirov, K.M. Firsov, V.S. Kozlov, M.V. Panchenko, Y.N. Ponomarev, B.A. Tikhomirov, Investigation of spectral dependence of shortwave radiation absorption by ambient aerosol using time-resolved photoacoustic technique, Opt. Eng. 44 (7) (2005) 071203-1–071203-11.

[7] A. Rosencwaig, A. Gersho, Theory of the photoacoustic effect with solids, App. Phys. 47 (1) (1976) 64–69.

[8] J.E. Carranza, B.T. Fisher, G.D. Yoder, D.W. Hahn, On line analysis of ambient air aerosols using laser induced breakdown spectroscopy, Spectrochim. Part B 56 (2001) 851–864.

[9] K.T. Rodolfa, D. Cremers, Capabilities of surface composition analysis using a long laser induced breakdown spectroscopy spark, Appl. Spectrosc. 58 (4) (2004) 367–375.

[10] P.O. Witze, High energy laser diagnostics for real time measurements of diesel particulate matter emissions, in: Proceedings of the Seventh International Congress on Optical Particle Characterization, Kyoto, Japan, August 2004.

[11] L.A. Melton, Soot diagnostics based on laser heating, Appl. Opt. 23 (13) (1984) 2201–2208.

[12] V. Kruger, C. Wahl, R. Hadef, K.P. Geigle, W. Stricker, M. Aigner, Comparison of laser induced incandescence method with scanning mobility particle sizer technique: the influence of probe sampling and laser heating on soot particle size distribution, Measure. Sci. Technol. 16 (2005) 1477–1486.

[13] C. Presser, A. Nazarian, Absorption coefficient measurements of carbonaceous-based aerosol particles using a laser driven thermal reactor, AIAA 2006-0379, in: Proceedings of 44th AIAA Aerospace Sciences Meeting and Exhibit, on CD, 2006.

[14] B.N. Taylor, C.E. Kuyatt, Guidelines for evaluating and expressing the uncertainty of nist measurement results, NIST Technical Note 1297, National Institute of Standards and Technology, Gaithersburg, Maryland, 1994.

[15] A. Nazarian, Thermal processes of interaction between charcoal and oxygen and ozone, Ph.D. Dissertation, Academy of Science of USSR, Institute of Thermophysics, 1985.

[16] D.R. Lide (Ed.), CRC Handbook of Chemistry and Physics, 87th ed., Taylor and Francis Group, Florida, 2006, pp. 4–90, 12–195, and 12–196, Also, http://www-ferp.ucsd.edu/LIB/PROPS/PANOS/cu.html.

[17] A. Nazarian, Thermal behavior of organic simulant wastes at high heating rates, in: 18th International Congress on Glass, San Francisco, California, July 1998.

[18] A. Nazarian, Study of the thermal behavior of high-level wastes using the laser driven thermal reactor, Waste Management, vol. 99, Tucson, Arizona, February 1999.

[19] C.F. Bohren, D.R. Huffman, Absorption and Scattering of Light by Small Particles, John Wiley, New York, 1983.

[20] A. Nazarian, B. Smirnov, Thermal characterization of mixed wastes, Waste Management, vol. 96, Tucson, Arizona, February 1996.

[21] F.P. Incropera, D.P. DeWitt, Introduction to Heat Transfer, Wiley, New York, 2002, pp. 240–243, 255.

[22] A. Nazarian, B. Smirnov, Characterization and modeling of the thermal processing of hazardous wastes and propellants, in: International Conference on Incineration and Thermal Treatment Technologies, Savannah, Georgia, May, 1996.

[23] A. Nazarian, On-line, input-stream process control sensor for high temperature process, in: International Conference on Controlling Industrial Emissions–Practical Experience, London, United Kingdom, 1997, pp. 149–155.

[24] A. Nazarian, Laser driven thermal reactor for hazardous waste stabilization, in: T.M. Gilliam, C.W. Carlton (Eds.), Stabilization and Solidification of Hazardous, Radioactive and Mixed Wastes, vol. 3, ASTM STP 1240, 1995, pp. 634–647.

[25] A. Nazarian, Heat transfer and energy balance of hanford waste tank 101-SY, in: S. Acharya, K. Annamalai, C. Presser, R.D. Skocypec (Eds.), Fire, Combustion and Hazardous Waste Processing, HTD, vol. 296, Am. Soc. Mech. Eng., New York, NY, 1994, pp. 177–187.

[26] D.R. Lide (Ed.), CRC Handbook of Chemistry and Physics, 87th ed., Taylor and Francis Group, Florida, 2006, pp. 1–42 (Section 5);
F.T. Wall, Chemical Thermodynamics, second ed., W.H. Freeman, San Francisco, 1965, pp. 431–442.

[27] Y. Takahashi, M. Murabayashi, Measurement of thermal properties of nuclear materials by laser flash method, J. Nuclear Sci. Technol. 12 (3) (1975) 133–144.

[28] J. Succc, Heat Transfer, Wm.C. Brown, Dubuque, Iowa, 1985, pp. 43–45.

[29] A. Nazarian, B. Smirnov, Measurement of thermal parameters of materials by laser methods, J. Thermophys. High Temperat. (Teplofizika vysokikh temperatur, in Russian) 29 (1991) 1032–1034.

[30] P.D. Jones, G. Teodorescu, R.A. Overfelt, Spectral-directional emittance of CuO at high temperatures, J. Heat Transfer 128 (2006) 382–388.